Solid-state nanopore sensing reveals conformational changes induced by a mutation in a neuron-specific tRNA^{Arg}

Shankar Dutt,[*,†] Lien B. Lai,[‡] Rahul Mehta,[¶,§] Buddini I. Karawdeniya,[‖,△] Y.M. Nuwan D.Y. Bandara,[*,⊥,∇] Andrew J. Clulow,[#] Sebastian Glatt,[¶,@] Venkat Gopalan,[*,‡] and Patrick Kluth[*,†]

†*Department of Materials Physics, Research School of Physics, Australian National University, Canberra, ACT 2601, Australia*

‡*Department of Chemistry and Biochemistry, Center for RNA Biology, The Ohio State University, Columbus, Ohio 43210, USA*

¶*Malopolska Centre of Biotechnology, Jagiellonian University, 30-387, Krakow, Poland*

§*Doctoral School of Exact and Natural Sciences, Jagiellonian University, 30-348, Krakow, Poland*

‖*Department of Electronics Materials Engineering, Research School of Physics, Australian National University, Canberra, ACT 2601, Australia*

⊥*Research School of Chemistry, Australian National University, Canberra, ACT 2601, Australia*

#*Australian Synchrotron, ANSTO, 800 Blackburn Road, Clayton, VIC 3168, Australia*

@*University of Veterinary Medicine Vienna, 1210 Vienna, Austria*

△*Current address: Department of Biomedical Engineering, The Ohio State University, Columbus, Ohio 43210, USA*

∇*Current address: Department of Chemistry and Biochemistry, The Ohio State University, Columbus, Ohio 43210, USA*

E-mail: shankar.dutt@anu.edu.au; bandara.7@osu.edu; gopalan.5@osu.edu; patrick.kluth@anu.edu.au

* Corresponding authors

Abstract

We demonstrate that solid-state nanopore sensing is a powerful single-molecule method for analyzing RNA conformational ensembles. As a model, we employed n-Tr20, a neuron-specific cytoplasmic $\mathrm{tRNA}^{\mathrm{Arg}}_{\mathrm{UCU}}$, whose C50U mutation is associated with neurodegeneration in C57BL/6J mice. Maturation of the $\mathrm{Tr20}^{\mathrm{C50U}}$ precursor is impaired as the mutation stabilizes a conformational ensemble different from the wild-type. To gain insights into how this mutation engenders structural differences, we used solid-state nanopore sensing for the real-time identification of metastable conformers that are not easily observable by ensemble methods. Ion-current traces recorded using an 8-nm nanopore revealed broad contours of the conformational landscape of n-Tr20/n-$\mathrm{Tr20}^{\mathrm{C50U}}$ $\pm$ Mg^{2+}. Additionally, small-angle X-ray scattering studies and cryo-EM analysis revealed structural plasticity even more than predicted from the nanopore-sensing data. Since dynamics undergird RNA (dys)function in cellular physiology and pathology, nanopore sensing to determine RNA conformational sampling is a valuable addition to the growing RNA structural analysis toolkit.

Graphical Abstract

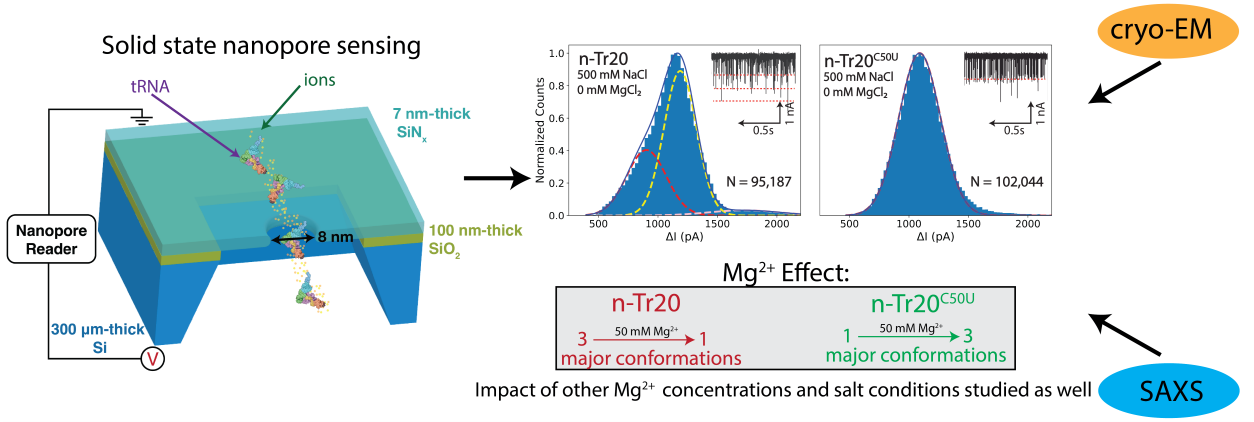

Single-molecule nanopore sensing reveals how C50U mutation in n-Tr20, a neuron-specific cytoplasmic $\mathrm{tRNA}^{\mathrm{Arg}}$ alters its conformational landscape (time-resolved) complemented by cryo-EM and SAXS analysis

Keywords

Solid-state nanopore sensing, single-molecule analysis, tRNA structure, conformational sampling, structural plasticity, SAXS, cryo-EM, time-resolved measurements

Introduction

The folding trajectory of structured RNAs typically entails a rugged energy landscape defined by several local minima, which reflect potential kinetic traps en route to a native fold [**1**]. Although chaperones and metal ions lower the energy barriers between intermediates and help convert metastable states to the final native structure, real-time observation of this conformational sampling has been largely intractable using conventional analytical methods. To address this limitation, we explore a nanopore-sensing approach and showcase its value with a transfer RNA (tRNA) as the model.

The most abundant cellular RNA (in molar amounts) is tRNA. These small non-coding RNAs (∼75 nt) deliver amino acids attached to their 3′ end to the ribosomes for protein synthesis [**1**]. Although often overlooked as a cause of diseases due to gene redundancy, there is increased appreciation that dysregulation of individual tRNAs could lead to neurodegenerative diseases, developmental defects, cancer, and hearing loss [**2**–**6**]. Given the extensive suite of post-transcriptional modifications (total ∼100, average of 13 per mammalian tRNA), this fine-tuning of tRNA structure and function in response to changing levels of cellular metabolites provides another tier of regulation [**7**–**11**]. However, understanding how genetic mutations or modifications influence RNA structural dynamics remains a formidable challenge, given the intrinsic propensity of RNAs to sample stable inter/intramolecular interactions and adopt alternative structures [**12**–**14**].

Traditionally, tRNAs have been studied employing ensemble methods, such as nuclear magnetic resonance spectroscopy [**15**, **16**] and X-ray crystallography [**17**]. Although these techniques have provided high-resolution structures, they do not capture metastable states

essential to understanding the tRNA structural dynamics, especially under different physiological conditions. On the other hand, single-molecule techniques such as single-molecule fluorescence resonance energy transfer (smFRET) and optical tweezer-based methodologies show promise for characterizing RNA dynamics, but their low-throughput precludes studies of large molecular populations [**18**].

Solid-state nanopore-enabled resistive pulse sensing (**Fig. 1a**) offers label-free monitoring of single-molecule biomolecular dynamics providing time-resolved structural information of the biomolecules and, as shown in the present study, could potentially become a valuable technique for studying tRNA conformational changes. By bridging the gap between detailed single-molecule insights and high-throughput data from hundreds of thousands of molecules (up to 10,000 translocation events/min [**19**]), solid-state nanopore sensing offers the advantages of both approaches, enabling robust statistical analysis and detailed conformational understanding at the level of individual molecules.

A solid-state nanopore is a nanofluidic device comprising a nanometer-scale channel that connects two electrolyte reservoirs. These nanochannels have been fabricated in insulating materials such as silicon nitride (SiN_x) [**19**–**21**], silicon dioxide (SiO_2) [**22**, **23**], hafnium oxide (HfO_x) [**24**, **25**], polymers [**26**, **27**] or two-dimensional (2D) materials such as graphene[**28**, **29**], and molybdenum disulfide [**30**]. Under an applied electro-potential bias, the flow of ions through the nanopore generates a baseline current. An event occurs when a (bio)molecule translocates through the pore and perturbs the ion flow, thereby causing current fluctuations that in turn are recorded as resistive or conductive pulses characteristic of the (bio)molecule. This current signature encodes information about the structure of the translocating (bio)molecule. Recent advances in thin-membrane fabrication by controlled etching or thinning [**19**, **31**, **32**], nanopore fabrication by the controlled breakdown method [**33**–**36**], and the use of machine learning [**37**–**41**] have paved the way to widespread adoption of solid-state nanopores for sensing and structural analysis of different molecules.

Solid-state nanopores (**Fig. 1a**) have been successfully used to probe the conformations

of proteins and their complexes [**37**, **42**, **43**] and study the flexibility/rigidity of enzymes [**44**]. Recently, solid-state nanopores have also shown promise in sensing RNA molecules [**45**, **46**]. These studies have yielded information on structure-function correlations that extend beyond those obtained from static crystallographic snapshots. Here, we employed nanopore sensing to study the structural changes of n-Tr20, a neuron-specific $tRNA^{Arg}$ whose C50U mutation is associated with neurodegeneration in C57BL/6J mice [**5**].

We investigated Mg^{2+}-dependent and time-resolved conformational dynamics of n-Tr20 and n-$Tr20^{C50U}$. To gain additional insights into the wide conformational space sampled by n-Tr20 and n-$Tr20^{C50U}$, we performed synchrotron-based small-angle X-ray scattering (SAXS) and used structural modeling to better understand the range of individual conformers and the basis for the nanopore measurements. Additionally, we employed cryo-EM analysis to complement our solid-state nanopore and SAXS analysis. By capturing data from $\sim 3 \times 10^6$ tRNAs, we show how solid-state nanopore-based resistive pulse sensing and analysis surpasses a key limitation of existing approaches and is a valuable tool to map the temporal structural properties of tRNAs and potentially other RNAs and RNA-protein complexes.

Experimental

Preparation of mature n-Tr20 and n-$Tr20^{C50U}$: The mature tRNA sequences were cloned downstream of the T7 promoter in pBT7 as described in our earlier work [**14**]. To generate transcripts by run-off in vitro transcription using T7 RNA polymerase, the DNA templates were amplified by PCR using the above clones and the primers F-ext (5′-CGAC GTTGTAAAACGACGGCCAG-3′) and pARGnoCCA-R (5′-CATCTCTGCCGGGACTC GAAC-3′). The transcripts were extensively dialyzed against water and then precipitated with sodium acetate and ethanol. After resuspension in water, the final RNA concentration was determined using a NanoDrop spectrophotometer and the specific extinction coefficient of the RNA at 260 nm.

Nanopore fabrication: Silicon nitride windows of 40 μm $\times$ 40 μm in size and of $\sim$ 7 nm thickness with a silicon dioxide underlayer of 100 nm thickness were fabricated using methods described before [**19**]. Nanopores in these windows were fabricated using the controlled breakdown method [**19**, **34**] by applying <1 V/nm voltage across the membrane. One molar KCl (pH 7) was used for nanopore fabrication. The voltage application ceased immediately upon the detection of a sharp increase in current, signaling the successful creation of a nanopore. To determine the dimensions of the crafted nanopore, we analyzed its open pore conductance. This objective was achieved by performing a linear fit of the current-voltage data, which were recorded using the eNPR-200 amplifier. The diameter of the pore was calculated using the following equation [**19**, **47**]:

$$G_0 = K \left(\frac{1}{\frac{\pi r^2}{L_0} + \left(\frac{\mu|\sigma|}{K} \cdot \frac{2\pi r}{L_0} \right)} + \frac{2}{\alpha \cdot 2r + \beta \cdot \frac{\mu|\sigma|}{K}} \right)^{-1} \tag{1}$$

where G_0, r, K, σ, μ, α, and β are, respectively, the open-pore conductance, nanopore radius, electrolyte conductivity, nanopore surface charge density, mobility of counterions proximal to the surface, and model-dependent parameters (both α and β are set to 2).

Nanopore data acquisition and analysis: The translocation measurements of the tRNA were performed in 5 mM Tris-HCl (pH 8) and 500 mM NaCl under an applied bias of 400 mV. Before translocation experiments, tRNA was refolded in water (95 °C for 3 min, 37 °C for 10 min) prior to addition of the electrolyte at the specified concentration. The samples were incubated for 30 min and the measurements were performed at $\sim$22 °C. Experiments were carried out after the incubation period and the time was set as t_0 when $MgCl_2$ was added (in the case of time-resolved experiments). 10 nM tRNA was used for translocation experiments. Data was acquired at 200 kHz sampling rate and low-pass filtered using a 35 kHz Butterworth filter [**37**]. For event extraction, we used the methodology detailed in our previous work, applying threshold values of at least five times the standard deviation of the baseline current in the analysis window [**37**]. For generating time-resolved

graphs, the data were segmented into 7-minute intervals, since this duration typically yielded approximately 10,000 events. For the analysis of these events, the histogram plots were subjected to Gaussian fitting based on machine learning to deconvolute the data.

Native polyacrylamide gel electrophoresis (nPAGE): 10 pM of either n-Tr20 or n-Tr20^{C50U} in water was incubated at 95 °C for 3 min and at 37 °C for 10 min before adding 5 mM Tris-HCl, (pH 8 at 22 °C), 0.5 M NaCl or KCl, and varying amounta of $MgCl_2$ to a final volume of 10 μL. The sample was then incubated at 37 °C for an additional 30 min. Subsequently, 3 μL of loading buffer [50% (v/v) glycerol, 0.05% (w/v) bromophenol blue, 0.05% (w/v) xylene cyanol] was added. TBM buffer (89 mM Tris base, 89 mM boric acid, 2 mM $MgCl_2$) was used to prepare a 5% (w/v) polyacrylamide (19:1 acrylamide:bis-acrylamide) gel and used as the running buffer for electrophoresis. The gels (17 cm width × 15 cm height) were electrophoresed at 180 V and 4 °C until the bromophenol blue dye reached the bottom. Gels were then stained with SYBR Gold (Invitrogen) in TBE buffer for 5 min and then scanned using a Typhoon phosphorimager (GE Healthcare) and the Cy2 imaging mode.

Small-angle X-ray scattering (SAXS): Consistent with the conditions of our nanopore experiments, 0.5 mg/mL of mature tRNA in water was incubated at 95°C for 3 minutes, followed by cooling at 37 °C for 5 minutes. Subsequently, 5 mM Tris-HCL (pH 8) and 500 mM NaCl were added, along with 0 mM or 50 mM $MgCl_2$. Transmission SAXS measurements were performed on the bioSAXS beamline of the Australian Synchrotron using X-rays with an energy of 12.4 keV, corresponding to a wavelength of 1 Å. Data collection was performed with an automated sample changer (CoFlow) and a Pilatus3X-2M detector (in a vacuum-movable detector system) with a pixel size of 172 μm^2. The sample-to-detector distance was calibrated at 3156 mm against a combination of silver behenate and LUDOX® colloidal silica particles used as a secondary standard. To mitigate radiation damage, a laminar sheath flow of the buffer solution was used along the capillary walls. Each sample (50 μL) underwent 20 acquisitions, each lasting 0.5 seconds throughout the injection of the sample. Data reduction

was performed using the pyFAI library[**48**] with a custom-written script. The reduced data were then averaged and buffer-only measurements subtracted.

The resulting scattering curves were analyzed using the ATSAS software suite[**49**]. To determine the radius of gyration, the linear region of $ln(\mathrm{I})$ *vs* q^2 was identified ($\mathrm{qR}_g < 1.3$) for each curve using Guinier analysis. Pairwise distance distribution functions were computed with GNOM from the ATSAS suite and subsequently utilized for *ab initio* shape modeling with DAMMIN, employing simulated annealing and a dummy-atom model. A total of 300 bead models were generated for each scattering curve and clustered using DAMAVER.

Ab initio modeling was performed via a simulated annealing process, involving random modifications to the identity of individual beads in the model, switching between particle atoms and solvent atoms or leaving them unchanged. After each step, the model was evaluated for its fit to the experimental data accounting for penalties for looseness or connectivity [**50**, **51**]. This approach facilitated the generation of different structural models for various conditions, and the conformational analysis revealed a good agreement between the static structural insights derived from SAXS and the information obtained from nanopore sensing and cryo-EM.

Electron microscopy: QUANTIFOIL® R 2/1 copper grids (200 mesh) were glow discharged using a Leica EM ACE 200 glow discharger (8 mA, 60 s). 3 μL of 34 μM (n-Tr20) or 54 μM (n-Tr20$^{\mathrm{C50U}}$) in assay buffer [20 mM HEPES (pH 7.5), 50 mM NaCl, 50 mM KCl, 1 mM $MgCl_2$,) were plunge-frozen using a Vitrobot Mark IV (Thermo Fisher Scientific) set to 100% humidity and 4 °C with the following blotting parameters: wait time 1 s, blot force 5 u and blot time 3 s. The datasets were collected on a 300 keV Titan Krios G3i (Thermo Fisher Scientific, Solaris, Poland) equipped with a Gatan BioQuantum energy filter and a Gatan K3 direct electron detector. The under-focus range was -0.9 to -2.1 µm for n-Tr20$^{\mathrm{C50U}}$ and -0.9 to -1.8 µm for n-Tr20. At each position, a total of 40 frames were collected that accumulated an overall dose of 40 $\mathrm{e}^{-}\mathrm{Å}^2$. The respective numbers of micrographs collected for each data set can be found in the Supplementary Table **1**. The pixel size used for both

datasets was 0.86 Å. (Note: The tRNAs used for cryo-EM studies included a 3'-CCA in contrast to the nanopore and SAXS studies.)

Image processing: All micrographs were subjected to motion correction using patch motion correction in Cryosparc (version 4.6.2) with default parameters with subsequent patch CTF estimation. The micrographs were then subjected to micrograph denoising using a pre-trained model and a grayscale normalization factor of 1 for further analysis. Blob picking was performed on a subset of micrographs to pick an initial set of particles. The particles were extracted and reference-free 2D classification was used to confirm the presence of RNA particles with the expected size. After validation of the selected particles, the entire data set was subjected to blob picking with the same parameters. Those classes of particles with a tRNA-like shape were used to create new 3D models using *ab initio* reconstruction. The particles falling into the classes containing features were pooled and again subjected to ab initio reconstruction (6 classes) to finally select the subset of particles with RNA-like features. Finally, classes exhibiting RNA features were refined by homogeneous refinement (HomoRef) [**52**]. The FSC correlation curves were calculated for each final reconstruction and the resolution was estimated using the gold standard FSC threshold of 0.143.

Results and Discussion

We used an ultra-thin SiN_x based solid-state nanopore membrane with 100 nm SiO_2 underlayer supported by Si [**19**] to study the conformational states of n-Tr20 and n-Tr20^{C50U} using resistive-pulse sensing (**Fig. 1a**, **1b**). To optimize the experimental conditions, we tested electrolyte salt concentrations ranging from 100 mM to 2000 mM to determine the lowest salt concentration that yields an acceptable signal-to-noise ratio (SNR) and a suitable rate of tRNA translocations. High salt concentrations are known to affect tRNA conformations [**53**], while low salt concentrations significantly reduce the translocation frequency through the nanopores. The results of our optimization studies (not shown) led to our choice of

500 mM NaCl for all subsequent experiments (unless indicated otherwise; some instances required the use of 500 mM KCl).

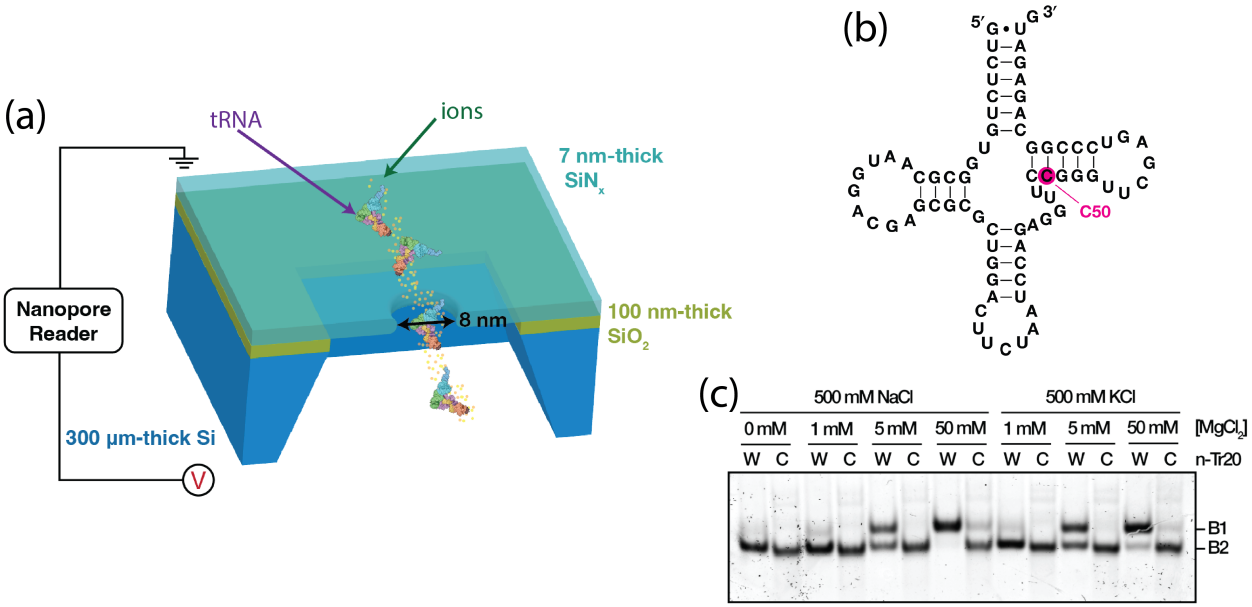

Figure 1: Use of a solid-state nanopore sensor and native PAGE to study tRNA conformational dynamics. (a) Schematic of tRNA translocation through a 7-nm-thick SiN_x membrane with a 8-nm diameter nanopore. A 100-nm-thick SiO_2 underlayer was used to reduce dielectric noise [**19**, **54**]. The layers are supported by a 300-μm thick silicon wafer. (b) Secondary structure of n-Tr20 with the C50U mutation depicted. (c) Native PAGE analysis of n-Tr20 (W) and $Tr20^{C50U}$ (C) folded in the indicated concentrations of $MgCl_2$ and either 500 mM NaCl or KCl. The tRNAs separated into two main bands, denoted as B1 and B2 (see text for details). It is likely that these bands represent conformational ensembles and not distinct species.

We and others have used native polyacrylamide gel electrophoresis (nPAGE) to investigate the presence of multiple conformations [**14**, **55**, **56**], which are distinguished based on their distinct electrophoretic mobilities. To maintain uniform conditions between different experiments in this study, we performed nPAGE experiments in $MgCl_2$ concentrations ranging from 0 mM to 50 mM and in either 500 mM NaCl or KCl (**Fig. 1c**). We found that n-Tr20 and n-$Tr20^{C50U}$, folded in the absence of Mg^{2+}, migrate as a single species (labeled B2). As $[Mg^{2+}]$ is increased in the refolding buffer, n-Tr20 transitions to a single slower-migrating species (B1). Because Mg^{2+} stabilizes the tertiary structure of tRNA, B1 is likely the native fold/ensemble [**14**]. However, a very small fraction of n-Tr20 was still in B2, the

non-native state/ensemble, even in 50 mM $MgCl_2$ and 500 mM KCl. It is possible that interactions with potassium ions (K^+) [**53**, **57**] account for this behavior. Unlike n-Tr20, n-Tr20^{C50U} shows at least two different mobilities even in 50 mM $MgCl_2$ (B1 and B2); this trend is maintained in the presence of 500 mM NaCl or 500 mM KCl (**Fig. 1c**). Thus, only a small fraction of n-Tr20^{C50U} adopts a native-like conformation/ensemble.

For nanopore experiments, selecting the optimal nanopore size and applied bias is crucial to (i) ensure a good SNR, (ii) reduce the blockage frequency during long-term measurements, and (iii) accommodate the dimensions of the tRNA molecule. Larger nanopores tend to produce lower SNR, whereas nanopores smaller than or comparable in size to the translocating (bio)molecule may cause stretching or distortion of molecular domains, leading to incorrect inferences about the (bio)molecule structure[**58**]. Similarly, high bias conditions can also induce the unfolding of the molecule during translocation [**59**]. Thus, nanopores ranging from 3.9 ± 0.4 nm to 11.9 ± 0.6 nm were tested to identify the optimal nanopore dimensions for the analysis of n-Tr20 and n-Tr20^{C50U} (**Fig. 2**).

Figure 2a shows representative ionic current traces of n-Tr20 translocations through pores of different sizes, while **Fig. 2b** plots the current-voltage (I-V) characteristics of these nanopores in 500 mM NaCl. The translocations were recorded at a sampling rate of 200 kHz and filtered at 35 kHz (determined as the optimal cutoff frequency [**37**]). No tRNA translocations were observed through nanopores with diameter ~ 3.9 nm, which is not unexpected, as the simulations (using CentroidFold [**60**] and RNAComposer [**61**]) predict that the smallest dimension of the tRNA is $\sim$5 nm. **Figure 2c** displays the histograms corresponding to the drop in current (ΔI) for each nanopore size for which translocations were observed. ΔI is a measure of volumetric occlusion by the tRNA analyte during its passage through the pore. When using a 5-nm diamter nanopore, two populations were observed, centering at approximately 300 pA and 630 pA; they likely correspond to collisions of tRNA molecules with the nanopore and and back deflections (300 pA) or the smaller of two populations of tRNA (discussed more below) translocating the nanopore (630 pA). With

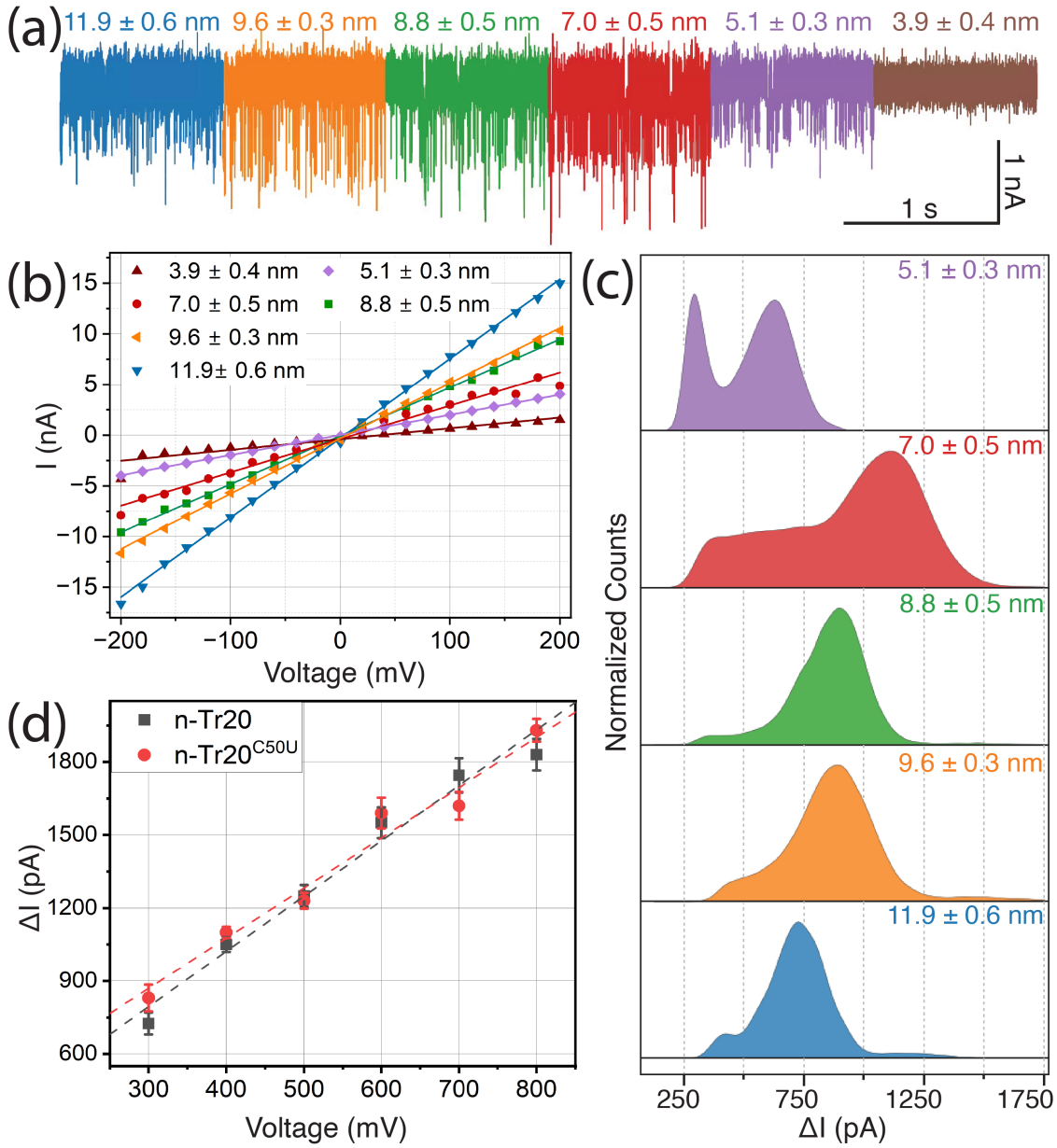

Figure 2: Investigation of optimal nanopore size and applied bias for tRNA experiments. (a) Representative current traces of n-Tr20 translocations through nanopores of varying diameters ranging from ∼4 to ∼12 nm. The measurements were conducted with 10 nM n-Tr20 in 5 mM Tris (pH 8) and 500 mM NaCl, with a bias of +400 mV. The corresponding open pore current-voltage traces for each pore size are shown in (b). The nanopore sizes were estimated using Equation 1 (see Methods). (c) Histograms illustrating the drop in ionic current (ΔI) when n-Tr20 molecules translocate through nanopores of varying sizes, highlighting the dependence of the current blockade results on pore diameters. (d) Observation of near-linear, voltage-dependent decrease in current (corresponding to the peak of the histogram, ΔI_{peak}) for n-Tr20 and n-Tr20^{C50U}. The dotted lines represent linear fits to the data.

a ∼7-nm nanopore, these populations with lower ΔI are still present. However, prevalent blockages observed suggest that many tRNA molecules have a size comparable to that of the nanopore diameter and encounter difficulty translocating through the nanopore. As the pore diameter increases from ∼7 to ∼11.9 nm, the major peak shifted to the left, a trend reflecting the increased ease of translocation by the two tRNA populations. Based on these findings, we selected nanopores of ∼8 nm for subsequent experiments. For nanopore sensing, the diameter of the pores should be close to the size of the translocating molecule for achieving optimal SNR; our choice of 8 nm which we determined empirically, is consistent with the maximum dimension of 8 nm deduced from the crystal structure of $tRNA^{Phe}$ [**62**, **63**].

We also observed a nearly linear relationship between the applied bias and ΔI_{peak} (ΔI values at the peak of the histogram) for both n-Tr20 and n-$Tr20^{C50U}$ (**Fig. 2d**). This correlation indicates that varying the applied bias does not significantly affect the experimental results. For all further experiments, we chose a bias of 400 mV as the standard operating condition.

To draw inferences on the structural ensemble of n-Tr20 and n-$Tr20^{C50U}$, we illustrate ΔI using histograms (the corresponding scatter plots are shown in the supplementary information, **Fig. S1**). Each histogram is derived from the analysis of tens of thousands of translocation events (**Fig. 3** lists the number of events). We previously showed that Mg^{2+} dictates the folds of n-Tr20 and n-$Tr20^{C50U}$ (**Fig. 1c**) [**14**]. Therefore, we first investigated the effect of Mg^{2+} (included during tRNA re-folding) on the nanopore translocation characteristics of n-Tr20 and n-$Tr20^{C50U}$. Our ΔI analysis (**Fig. 3a**) revealed three distinguishable populations for n-Tr20 in the absence of Mg^{2+} that collapse to a single population upon the addition of 50 mM Mg^{2+}(**Fig. 3b**) (even in 5–10 mM Mg^{2+}, not shown). This observation suggests that all of the wild-type tRNA is folded to adopt a native fold/ensemble. In contrast, n-$Tr20^{C50U}$ switches from one to three different populations when exposed to 50 mM Mg^{2+}, as evidenced by the broadening of the distribution of current blockade amplitudes (**Figs. 3c**, **3d**). Although a triple Gaussian function was used to fit the data obtained

from both n-Tr20 (0 mM Mg^{2+}) and n-Tr20^{C50U} (50 mM Mg^{2+}), the overall distribution is narrower in the latter (see below).

Our finding of three distinct ΔI populations (n-Tr20 in 0 mM Mg^{2+}), more than the two apparent states detected by nPAGE (**Fig. 1c**), highlights the ability of nanopore sensing to better identify the conformational ensemble in solution. The native gel mobility of each of the RNA conformers is dictated by the RNA shape/size and the size of the polyacrylamide pores, similar to the nanopore measurements that reflect the cross-sectional area of the different tRNA structural states. However, the caging effect of the native gel matrix may have narrowed the true conformational space.

We previously postulated that while n-Tr20 (in the absence of Mg^{2+}) samples both native and non-native conformational ensembles, Mg^{2+} addition leads to a bias in favor of the native state. In contrast, n-Tr20^{C50U} appears to be trapped in non-native ensemble state(s), as reflected by our finding that $\sim$75% of pre–n-Tr20^{C50U} being intractable to 5′ processing by RNase P even in 5 mM Mg^{2+} [**14**]. The ΔI histograms (**Fig. 3**) are consistent with this scenario. Furthermore, despite the conformational heterogeneity of n-Tr20^{C50U} in the presence of Mg^{2+}, the higher ΔI observed for n-Tr20^{C50U} relative to n-Tr20 (**Figs. 3c**, **3d**) suggests a predominantly larger-sized conformation for the former. Some of the secondary structures predicted for n-Tr20^{C50U} suggest longer dimensions compared to those for n-Tr20 (**Fig. S2**). Considering the range of potential conformations, we propose that both n-Tr20 and n-Tr20^{C50U} are capable of adopting a few different structures [**14**]. The expectation of larger conformations for n-Tr20^{C50U} aligns with small-angle X-ray scattering (SAXS) and cryo-EM observations (**Fig. 4**, Supplementary Figures **S8, S9**), which leverage nanoscale density differences to infer size and shape distributions of the tRNAs (see below).

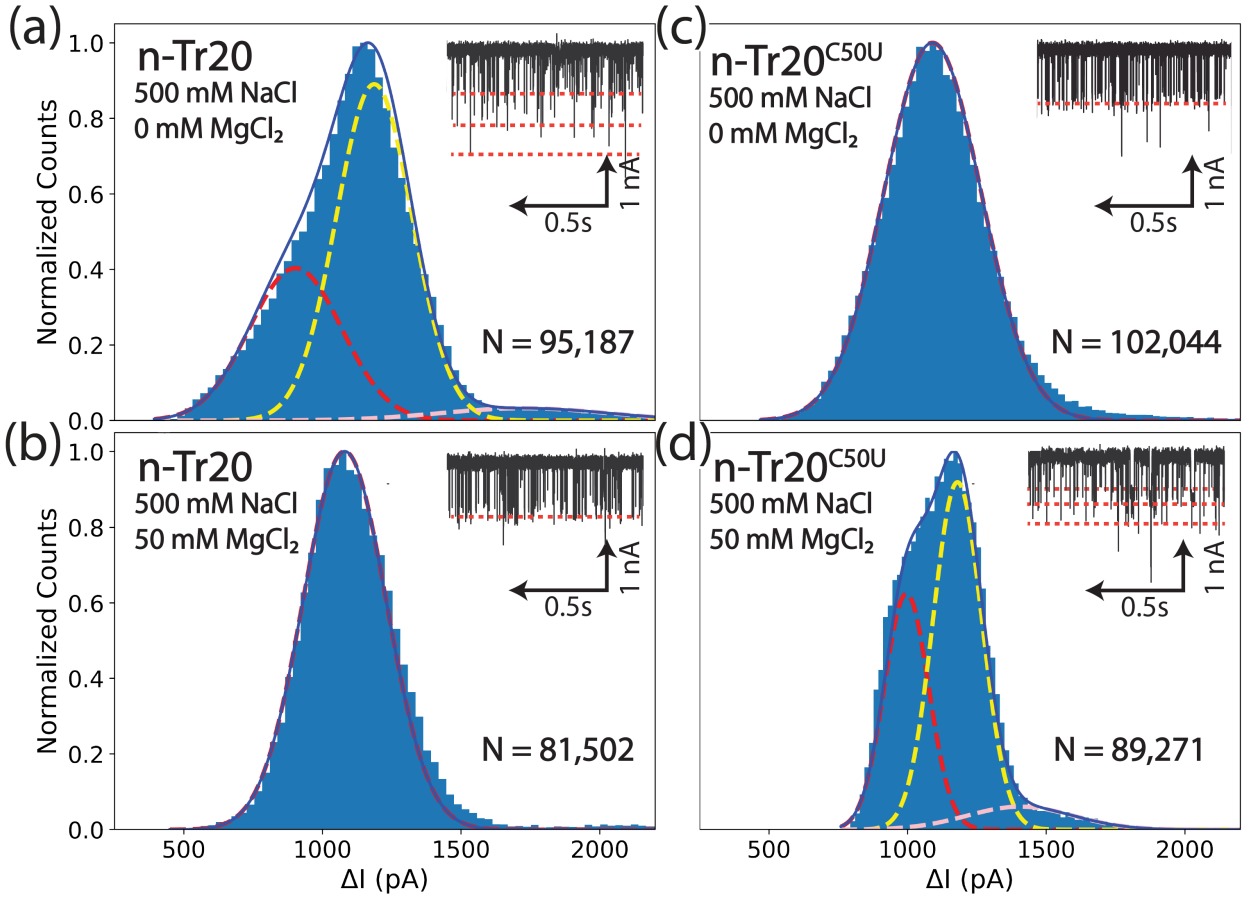

Figure 3: Solid-state nanopore measurements of n-Tr20 and n-Tr20^{C50U}. Comparative histograms of the ionic current reduction (ΔI) observed during nanopore-sensing experiments for n-Tr20 (a, b) and n-Tr20^{C50U} (c, d). Insets display representative ionic current-time traces corresponding to translocation events for each condition indicated. N denotes the total number of events measured and used to generate the histograms. n-Tr20 exhibits three distinct populations (represented by gaussian peaks) when measured in the absence of $MgCl_2$, but coalesces into a single population under 50 mM $MgCl_2$. In contrast, the n-Tr20^{C50U} exists as a single population in the absence of $MgCl_2$, but exhibits three distinct conformations under 50 mM $MgCl_2$.

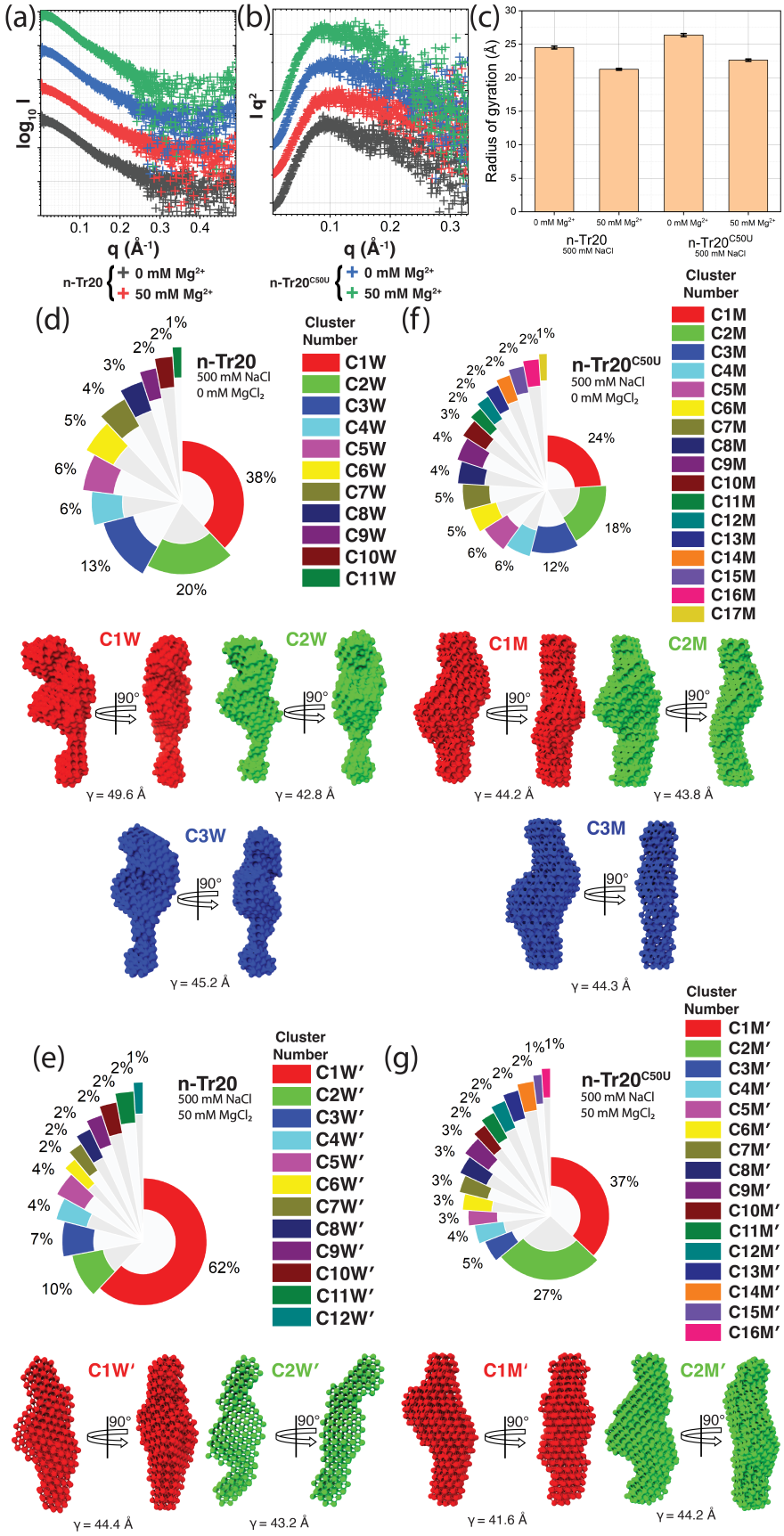
(a)
(b)
(c)
log10 I
I q²
q (Å⁻¹)
n-Tr20 0 mM Mg2+ 50 mM Mg2+
n-Tr20C50U 0 mM Mg2+ 50 mM Mg2+
Radius of gyration (Å)
n-Tr20 500 mM NaCl
n-Tr20C50U 500 mM NaCl
(d)
n-Tr20 500 mM NaCl 0 mM MgCl2
Cluster Number
C1W C2W C3W C4W C5W C6W C7W C8W C9W C10W C11W
(f)
n-Tr20C50U 500 mM NaCl 0 mM MgCl2
C1M C2M C3M C4M C5M C6M C7M C8M C9M C10M C11M C12M C13M C14M C15M C16M C17M
C1W γ = 49.6 Å
C2W γ = 42.8 Å
C1M γ = 44.2 Å
C2M γ = 43.8 Å
C3W γ = 45.2 Å
C3M γ = 44.3 Å
(e)
n-Tr20 500 mM NaCl 50 mM MgCl2
C1W′ C2W′ C3W′ C4W′ C5W′ C6W′ C7W′ C8W′ C9W′ C10W′ C11W′ C12W′
(g)
n-Tr20C50U 500 mM NaCl 50 mM MgCl2
C1M′ C2M′ C3M′ C4M′ C5M′ C6M′ C7M′ C8M′ C9M′ C10M′ C11M′ C12M′ C13M′ C14M′ C15M′ C16M′
C1W′ γ = 44.4 Å
C2W′ γ = 43.2 Å
C1M′ γ = 41.6 Å
C2M′ γ = 44.2 Å

Figure 4: Small-angle X-ray scattering analysis of n-Tr20 and n-Tr20^{C50U} tRNA. (a) Scattering intensities as a function of scattering vector and (b) Kratky plots (Iq^2 vs. q) for n-Tr20 and n-Tr20^{C50U} with and without the addition of 50 mM Mg^{2+} to a solution containing 5 mM Tris-HCl (pH 8) and 500 mM NaCl. The plots in (a) and (b) are offset vertically for clarity (see **Fig. S3-S5** for detailed plots). (c) Bar graph summarizing the radius of gyration (R_g) for the different samples, determined from the linear region of ln(I) vs. q^2 using Guinier analysis. Conformational clusters for n-Tr20 and n-Tr20^{C50U} in 500 mM NaCl, with and without Mg^{2+}, are depicted in (d)–(g). Pie charts indicate the relative abundance of structural clusters, based on 300 models constructed using DAMMIN analysis and clustered with DAMAVER. Only clusters with more than 10% representation are shown; additional clusters are presented in the Supporting Information (**Figs. S6–S7**). The final renditions were generated using ChimeraX [**64**]. The cross-sectional diameter γ for the cluster representatives is also listed).

To complement the solid-state nanopore measurements and examine the tertiary structures of n-Tr20 and n-Tr20^{C50U} under different conditions, we employed SAXS. A tRNA concentration of 0.5 mg/mL ($\sim$20 μM) was used in these studies. **Figure 4a** presents the PRIMUS plots of reduced data, while **Figure 4b** displays the Kratky plots for n-Tr20 and n-Tr20^{C50U} in 5 mM Tris buffer (pH 8), 500 NaCl with and without 50 mM $MgCl_2$. PRIMUS-based quality analysis confirmed the absence of significant aggregation or interparticle interference (**Fig 4a**) [**65**]. The sharply bent profile in the Kratky plots indicates that the tRNA remain folded in solution (**Fig 4b**) [**66**]. Using these data, we calculated the radius of gyration (R_g) and found that it decreased by approximately 13% and 14% for n-Tr20 and n-Tr20^{C50U}, respectively, upon the addition of Mg^{2+}, reflecting structural compaction (**Fig 4c**). Furthermore, the R_g values for n-Tr20^{C50U} were $\sim$8% higher than those for n-Tr20, with and without Mg^{2+}, consistent with the predictions of our model and the nanopore measurements.

Despite the fact that SAXS data represent scattering by randomly oriented tRNA molecules present in multiple conformations, bead modeling-based shape reconstruction is useful for understanding conformational plasticity, which in turn can help to better understand the nanopore-sensing data. Therefore, we performed *ab initio* modeling using the DAMMIN package of the ATSAS software suite[**49**]. For each condition (n-Tr20 $\pm$ Mg^{2+};n-

Tr20^{C50U} ± Mg^{2+}), 300 independent models were generated using DAMCLUST[**49**]. This approach yielded 11 (C1W–C11W) and 17 (C1M–C17M) conformational clusters, respectively, for n-Tr20 and n-Tr20^{C50U} without Mg^{2+} and 12 (C1W′–C12W′) and 16 (C1M′–C16M′) clusters were identified for n-Tr20 and n-Tr20^{C50U} in the presence of 50 mM Mg^{2+} (**Fig 4**; Supplementary Figs.**S6 and S7**). Representative 3D structures of the major conformations (C1W–C3W, C1W′–C2W′, C1M–C3M, C1M′–C2M′) are also provided in Supplementary Videos **1**–**8**. These visualizations, rendered using ChimeraX [**67**], depict the tRNA structures under two rotational perspectives, along with their cross-sectional diameters.

Single particle cryo-EM has emerged as a useful tool to study the dynamic three-dimensional structures of folded RNA molecules [**68**]. In addition to different larger assemblies of RNAs [**69**], we and others have recently shown that the shape of small folded RNAs, such as tRNAs, can be studied by cryo-EM [**70**–**74**]. To further substantiate the conformational differences between n-Tr20 and n-Tr20^{C50U}, we prepared cryo-EM grids of the *in vitro* transcribed and refolded tRNA samples. The buffer used contained 20 mM HEPES (pH 7.5), 50 mM KCl, and 50 mM NaCl. 1 mM $MgCl_2$ was added after the refolding process was complete. We collected single particle datasets (Supplementary Table **1**), analyzed detected particle stacks, and reconstructed the coulomb density maps of individual classes of molecules (Supplementary Figures **S8 and S9**). Despite the limited resolution, the results show that basically all of the ∼250,000 detected n-Tr20 particles fall into different canonical tRNA shape classes that show a high degree of structural heterogeneity. In contrast, the ∼170,000 detected particles n-Tr20^{C50U} can be classified into both L-shaped molecules and elongated particles that resemble the alternative conformation that we had postulated previously [**14**] (Supplementary Figure **S2**) and complement and confirm the distribution of conformational differences between n-Tr20 and n-Tr20^{C50U} obt ained by solid-state nanopore sensing and SAXS.

These low-resolution shape reconstructions from SAXS and cryo-EM of n-Tr20 and n-Tr20^{C50U} are instructive. In particular, our data are consistent with the idea that muta-

tions or modifications in RNA change the RNA structural ensemble from one distribution to another by altering fractional contributions of different conformers [**75**]. Although the cryo-EM maps obtained have too low resolution to reliably fit molecular models for the two tRNA species and it remains to be shown which specific atomic changes lead to the formation of an alternative conformation in n-Tr20$^{\mathrm{C50U}}$, these analyses agree with our postulates. Furthermore, the SAXS and cryo-EM data provide cross-validation and help better understand the nanopore-sensing data. Consistent with the R_g measurements from SAXS, the conformational cross-sectional diameters (γ) decreased with the addition of Mg^{2+}.

For n-Tr20, the three major conformations observed in the absence of Mg^{2+} had γ values ranging from ∼43 Å to ∼50 Å, consistent with the distinct ΔI populations observed in nanopore measurements. Upon addition of Mg^{2+}, two major conformations were identified: C1W′ (62% of all models) and C2W′ (10% of all models), although only a single conformation was observed in nanopore measurements. This discrepancy may be due to the similar γ values of C1W'and C2W', as the ΔI values in the nanopore experiments reflect volumetric exclusion rather than fine structural details. Further insights could be obtained by analyzing the shape of nanopore signal events, but this undertaking is beyond the scope of this study. Unlike n-Tr20, three major conformations were identified for n-Tr20$^{\mathrm{C50U}}$ in the absence of Mg2+, although only a single conformation was observed in nanopore measurements. The proximity of the γ values for three conformations could explain why only a single conformational state is detected in nanopore measurements. With the addition of Mg^{2+}, two major conformations were observed for n-Tr20$^{\mathrm{C50U}}$: C1M′ and C2M′, which had different γ values. Interestingly, there were other clusters with smaller fractions of the total number of models considered that encompass a wider range of γ values suggesting greater structural plasticity with the mutant and in agreement with the nanopore ΔI results (**Fig. 3**).

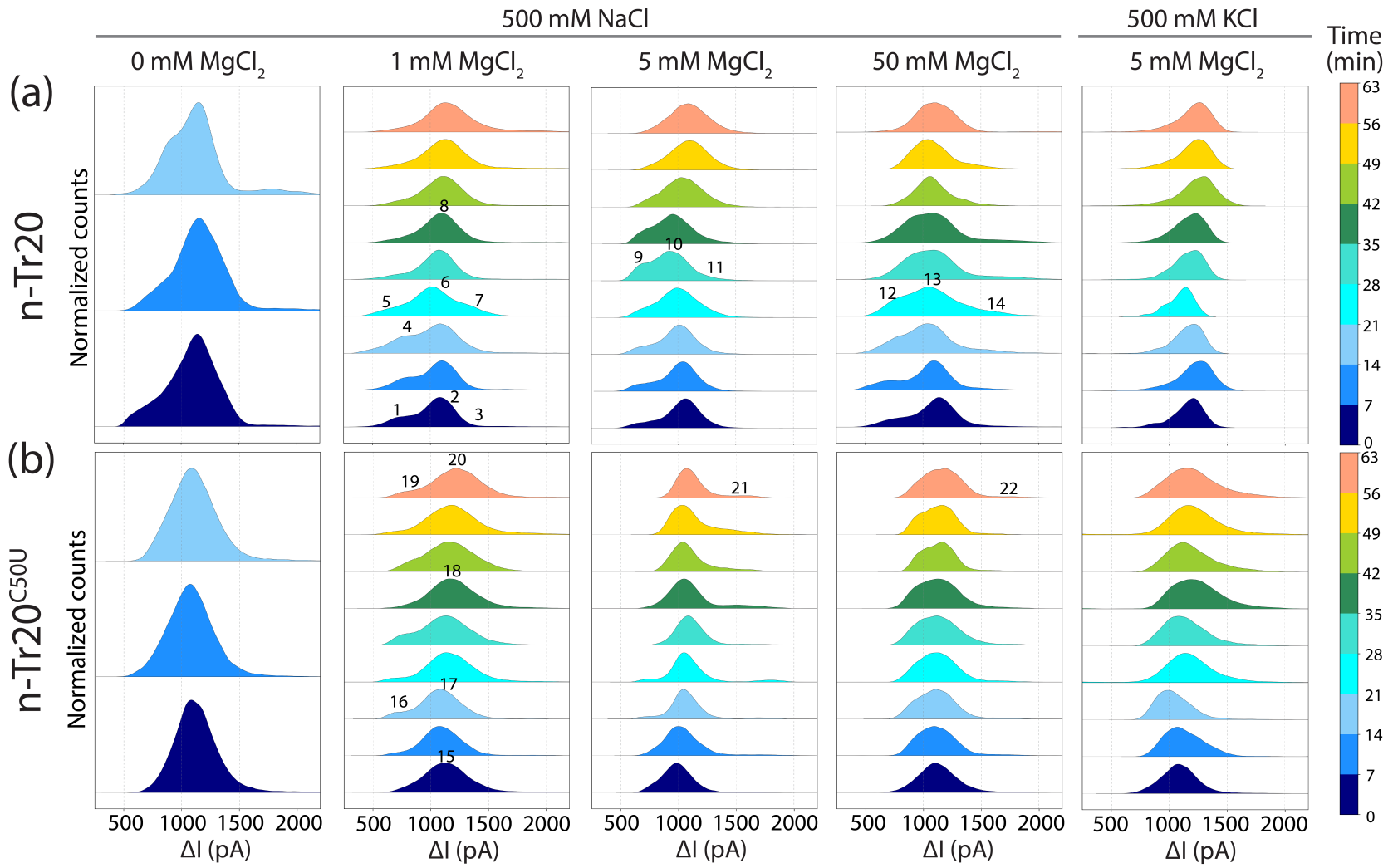

Figure 5: Time-resolved conformational changes of n-Tr20 and n-Tr20^{C50U}. (a) Time-resolved assessments of structural alterations in n-Tr20 and n-Tr20^{C50U} in different concentrations of $MgCl_2$ (as indicated) and either 500 mM NaCl or KCl as the electrolyte. Each histogram represents a 7-min measurement. Only the first three measurements (0-21 min) are shown for tRNAs without $MgCl_2$, as we observed minimal changes with time. These measurements were repeated multiple times to confirm the reproducibility of the temporal changes.

Solid-state nanopores not only detect the presence of different conformations within a sample solution but can also provide insights into the time-resolved structural changes of biomolecules under varying conditions. To explore this capability, we investigated the utility of nanopores for capturing time-resolved tRNA conformational dynamics. In these experiments, the tRNAs were re-folded in 5 mM Tris-HCl and 500 mM NaCl, and then 1, 5 or 50 mM $MgCl_2$ were added just before (t=0) nanopore measurements that were taken over a 60-min period. In the presence of 1mM Mg^{2+} and 500 mM NaCl, n-Tr20 initially ($t \leq 14$ min) displayed three peaks (peaks 1–3) in the ΔI profile (**Fig. 5a**), indicative of two major conformations and one minor conformation.

Over time, the fraction of the peak corresponding to a lower ΔI value (peak 4) increased, followed by the emergence of an intermediate conformation (peak 7) and redistribution among two lower ΔI peaks (peaks 5 and 6). Gradually, these three conformations merged into a single stable conformation (peak 8). A similar pattern of metastable intermediates was observed in the presence of 5 mM and 50 mM Mg^{2+} (peaks 9–14). In agreement with our previous observation of Mg^{2+}-induced structural compaction (**Fig. 3**, **4**), we also observe a tighter ΔI profile with increasing Mg^{2+} concentration (**Fig. 5**).

The conformational dynamics of n-Tr20^{C50U} (**Fig. 5b**) differed significantly from that of n-Tr20. At $t \leq 14$ min, n-Tr20^{C50U} in 1 mM Mg^{2+} a single major peak was observed (peak 15). Interestingly, this single population bifurcated (peaks 16 and 17), eventually collapsing into a single population (peak 18), before redistributing into two major populations (peaks 19 and 20). Following stabilization ($t > 40$ min) in 5 and 50 mM Mg^{2+}, higher-ΔI peaks (peaks 21 and 22) were observed, indicative of a larger-sized conformation compared to n-Tr20. These results exemplify the notion that RNA conformers can equilibrate with one another over minutes/hours [**1**]. As Mg^{2+} is increased from 1 to 5 to 50 mM, a broader range of ΔI range is apparent. These data are consistent with the view that Mg^{2+}-mediated charge screening might permit local conformational relaxation and thus flexural strength [**76**].

To further investigate the effects of Mg^{2+} concentration and electrolyte chemistry (NaCl versus KCl) on tRNA conformational dynamics, we employed native-PAGE and solid-state nanopore measurements (**Figs. 1c** and **5**). Interestingly, KCl induced structural changes more rapidly than NaCl, as evidenced by the stabilization of the ΔI values in a shorter time frame. This behavior probably reflects the ability of Mg^{2+}, which is essential for tertiary folding, to outcompete loosely bound K^+ ions more effectively [**53**, **76**]. These results demonstrate that nanopore sensing is a powerful tool for detecting conformational sampling driven by different ions.

Conclusions

Our findings highlight the utility of solid-state nanopore sensing for capturing time-resolved structural changes of tRNA species. As demonstrated here, solid-state nanopore measurements, as a single-molecule method, offer near-ensemble-level characterization of RNA structures, with potential for both basic and applied research. For instance, it should be possible to assess structural homogeneity of RNA samples prepared for cryo-EM studies or as therapeutics for different diseases. Because solid-state nanopore sensing is particularly effective under high-salt conditions, it is well-suited for studies of biomolecules from halophiles or those that require salt for stabilizing functional folds. Also, even at moderate throughput, nanopore sensing-based screening approaches could help identify small molecules that alter RNA conformational equilibria. As a first step in our efforts to build a picture of the conformational ensembles sampled by a tRNA under different solution conditions, we complemented nanopore measurements with native PAGE analysis, SAXS studies and cryo-EM analysis. Looking ahead, coupling time resolved-nanopore sensing, SAXS and cryo-EM offer exciting prospects for obtaining structural information over wide-ranging time and length scales. We are buoyed by the prospects of using nanopores for illuminating the "dark space" in RNA folding, but we recognize that this potential will be realized only when different

conformers identified in ΔI histograms are efficiently captured and analyzed using smFRET, native mass spectrometry, or structure-probing methods.

Acknowledgement

Part of this work was performed on the BioSAXS beamline at the Australian Synchrotron, ANSTO. **SD** acknowledges AINSE PGRA and Australian Government RTP. **LL** and **VG** acknowledges support from the National Institutes of Health (NS-096600 to Susan Ackerman and VG), the American Heart Association (23IPA1054097 to Susan Cole and VG), and the Behrman Research Fund (to VG). **PK**, **BK**, and **NB** acknowledge the ANU Grand Challenge 'Our Health in Our Hands' (OHIOH). Research funding for this study was provided by the European Research Council (ERC) under the European Union's Horizon 2020 research and innovation program grant No. 101001394 (**SG**). The work is supported by the Polish Ministry and Higher Education project: "Support for research and development with the use of research infrastructure of the National Synchrotron Radiation Centre SOLARIS" under contract nr 1/SOL/2021/2. The authors gratefully acknowledge the Polish high-performance computing infrastructure PLGrid (HPC Center: ACK Cyfronet AGH) for providing computer facilities and support within the computational grant no. PLG/2023/016097 (**RM**).

References

[**1**] Herschlag, D., Bonilla, S., and Bisaria, N. (2018). The story of RNA folding, as told in epochs. Cold Spring Harbor Perspectives in Biology **10**, a032433. `https://doi.org/10.1101/cshperspect.a032433`.

[**2**] Qiu, X., Yu, H., Karunakaran, M., Pradeep, N., Nunes, S. P., and Peinemann, K.-V. (2013). Selective separation of similarly sized proteins with tunable nanoporous block

copolymer membranes. ACS Nano **7**, 768–776. https://doi.org/10.1021/nn305073e.

[**3**] Orellana, E. A., Siegal, E., and Gregory, R. I. (2022). tRNA dysregulation and disease. Nature Reviews Genetics **23**, 651–664. https://doi.org/10.1038/s41576-022-00501-9.

[**4**] Coller, J., and Ignatova, Z. (2024). tRNA therapeutics for genetic diseases. Nature Reviews Drug Discovery **23**, 108–125. https://doi.org/10.1038/s41573-023-00829-9.

[**5**] Ishimura, R., Nagy, G., Dotu, I., Zhou, H., Yang, X.-L., Schimmel, P., Senju, S., Nishimura, Y. (2014). Ribosome stalling induced by mutation of a CNS-specific tRNA causes neurodegeneration. Science **345**, 455–459. https://doi.org/10.1126/science.1249749.

[**6**] Levinger, L., and Serjanov, D. (2012). Pathogenesis-related mutations in the T-loops of human mitochondrial tRNAs affect 3 end processing and tRNA structure. RNA Biology **9**, 283–291. https://doi.org/10.4161/rna.19025.

[**7**] Zhang, W., Foo, M., Eren, A. M., and Pan, T. (2022). tRNA modification dynamics from individual organisms to metaepitranscriptomics of microbiomes. Molecular Cell **82**, 891–906. https://doi.org/10.1016/j.molcel.2021.12.007.

[**8**] Novoa, E. M., Pavon-Eternod, M., Pan, T., and Ribas de Pouplana, L. (2012). A role for tRNA modifications in genome structure and codon usage. Cell **149**, 202–213. https://doi.org/10.1016/j.cell.2012.01.050.

[**9**] Roh, J. H., Tyagi, M., Briber, R. M., Woodson, S. A., and Sokolov, A. P. (2011). The dynamics of unfolded versus folded tRNA: The role of electrostatic interactions. Journal of the American Chemical Society **133**, 16406–16409. https://doi.org/10.1021/ja207667u.

[**10**] Zhang, M., and Lu, Z. (2025). tRNA modifications: greasing the wheels of translation and beyond. RNA Biology **22**, 1–25. https://doi.org/10.1080/15476286.2024.2442856.

[**11**] Cappannini, A., Ray, A., Purta, E., Mukherjee, S., Boccaletto, P., Moafinejad, S. N., Lechner, A., Barchet, C. (2024). MODOMICS: a database of RNA modifications and related information. 2023 update. Nucleic Acids Research **52**, D239–D244. https://doi.org/10.1093/nar/gkad1083.

[**12**] Volkov, I. L., Lindén, M., Aguirre Rivera, J., Ieong, K.-W., Metelev, M., Elf, J., and Johansson, M. (2018). tRNA tracking for direct measurements of protein synthesis kinetics in live cells. Nature Chemical Biology **14**, 618–626. https://doi.org/10.1038/s41589-018-0063-y.

[**13**] Šponer, J., Bussi, G., Krepl, M., Banáš, P., Bottaro, S., Cunha, R. A., Gil-Ley, A., Pinamonti, G. (2018). RNA structural dynamics as captured by molecular simulations: A comprehensive overview. Chemical Reviews **118**, 4177–4338. https://doi.org/10.1021/acs.chemrev.7b00427.

[**14**] Lai, L. B., Lai, S. M., Szymanski, E. S., Kapur, M., Choi, E. K., Al-Hashimi, H. M., Ackerman, S. L., and Gopalan, V. (2022). Structural basis for impaired 5 processing of a mutant tRNA associated with defects in neuronal homeostasis. Proceedings of the National Academy of Sciences **119**, e2119529119. https://doi.org/10.1073/pnas.2119529119.

[**15**] Marušič, M., Toplishek, M., and Plavec, J. (2023). NMR of RNA - Structure and interactions. Current Opinion in Structural Biology **79**, 102532. https://doi.org/10.1016/j.sbi.2023.102532.

[**16**] Kimura, S., Dedon, P. C., and Waldor, M. K. (2020). Comparative tRNA sequencing and RNA mass spectrometry for surveying tRNA modifications. Nature Chemical Biology **16**, 964–972. https://doi.org/10.1038/s41589-020-0558-1.

[**17**] Clark, B. F. (2001). The crystallization and structural determination of tRNA. Trends in Biochemical Sciences **26**, 511–514. https://doi.org/10.1016/S0968-0004(01)01910-7.

[**18**] Niu, X., Xu, Z., Zhang, Y., Zuo, X., Chen, C., and Fang, X. (2023). Structural and dynamic mechanisms for coupled folding and tRNA recognition of a translational T-box riboswitch. Nature Communications **14**, 7394. https://doi.org/10.1038/s41467-023-43232-z.

[**19**] Dutt, S., Karawdeniya, B. I., Bandara, Y. M. N. D. Y., Afrin, N., and Kluth, P. (2023). Ultrathin, high-lifetime silicon nitride membranes for nanopore sensing. Analytical Chemistry **95**, 5754–5763. https://doi.org/10.1021/acs.analchem.3c00023.

[**20**] Vlassiouk, I., Siwy, Z. S., Dmitriev, S. N., Apel, P. Y., and Healy, K. (2009). Versatile ultrathin nanoporous silicon nitride membranes. Proceedings of the National Academy of Sciences **106**, 21039–21044. https://doi.org/10.1073/pnas.0911450106.

[**21**] Chernev, A., Teng, Y., Thakur, M., Boureau, V., Navratilova, L., Cai, N., Chen, T.-H., Wen, L. (2023). Nature-inspired stalactite nanopores for biosensing and energy harvesting. Advanced Materials **35**, 2302827. https://doi.org/10.1002/adma.202302827.

[**22**] Kiy, A., Dutt, S., Notthoff, C., Toimil-Molares, M. E., Kirby, N., and Kluth, P. (2023). Highly rectifying conical nanopores in amorphous SiO_2 membranes for nanofluidic osmotic power generation and electroosmotic pumps. ACS Applied Nano Materials **6**, 8564–8573. https://doi.org/10.1021/acsanm.3c00960.

[**23**] Dutt, S., Notthoff, C., Wang, X., Trautmann, C., Mota-Santiago, P., and Kluth, P. (2023). Annealing of swift heavy ion tracks in amorphous silicon dioxide. Applied Surface Science **628**, 157370. https://doi.org/10.1016/j.apsusc.2023.157370.

[**24**] Larkin, J., Henley, R., Bell, D. C., Cohen-Karni, T., Rosenstein, J. K., and Wanunu, M. (2013). Slow DNA transport through nanopores in hafnium oxide membranes. ACS Nano **7**, 10121–10128. https://doi.org/10.1021/nn404326f.

[**25**] Emmerich, T., Teng, Y., Ronceray, N., Lopriore, E., Chiesa, R., Chernev, A., Artemov, V., Di Ventra, M. (2024). Nanofluidic logic with mechano–ionic memristive switches. Nature Electronics. https://doi.org/10.1038/s41928-024-01137-9.

[**26**] Dutt, S., Apel, P., Lizunov, N., Notthoff, C., Wen, Q., Trautmann, C., Mota-Santiago, P., Kirby, N. (2021). Shape of nanopores in track-etched polycarbonate membranes. Journal of Membrane Science **638**, 119681. https://doi.org/10.1016/j.memsci.2021.119681.

[**27**] Kececi, K., Kaya, D., and Martin, C. R. (2021). Resistive-pulse sensing of DNA with a polymeric nanopore sensor and characterization of DNA translocation. ChemNanoMat. https://doi.org/10.1002/cnma.202100424.

[**28**] Merchant, C. A., Healy, K., Wanunu, M., Ray, V., Peterman, N., Bartel, J., Fischbein, M. D., Venta, K. (2010). DNA translocation through graphene nanopores. Nano Letters **10**, 2915–2921. https://doi.org/10.1021/nl101046t.

[**29**] Kececi, K., and Dinler, A. (2024). Review—Recent applications of resistive-pulse sensing using 2D nanopores. Journal of The Electrochemical Society **171**, 037505. https://doi.org/10.1149/1945-7111/ad2d18.

[**30**] Ke, J.-A., Garaj, S., and Gradečak, S. (2019). Nanopores in 2D MoS_2 : Defect-mediated formation and density modulation. ACS Applied Materials & Interfaces **11**, 26228–26234. https://doi.org/10.1021/acsami.9b03531.

[**31**] Yanagi, I., and Takeda, K.-i. (2021). Sub-10-nm-thick SiN nanopore membranes fabricated using the SiO_2 sacrificial layer process. Nanotechnology **32**, 415301. https://doi.org/10.1088/1361-6528/ac10e3.

[**32**] Yamazaki, H., Hu, R., Zhao, Q., and Wanunu, M. (2018). Photothermally assisted thinning of silicon nitride membranes for ultrathin asymmetric nanopores. ACS Nano **12**, 12472–12481. https://doi.org/10.1021/acsnano.8b06805.

[**33**] Briggs, K., Kwok, H., and Tabard-Cossa, V. (2014). Automated fabrication of 2-nm solid-state nanopores for nucleic acid analysis. Small **10**, 2077–2086. https://doi.org/10.1002/smll.201303602.

[**34**] Waugh, M., Briggs, K., Gunn, D., Gibeault, M., King, S., Ingram, Q., Jimenez, A. M., Berryman, S. (2020). Solid-state nanopore fabrication by automated controlled breakdown. Nature Protocols **15**, 122–143. https://doi.org/10.1038/s41596-019-0255-2.

[**35**] Kwok, H., Briggs, K., and Tabard-Cossa, V. (2014). Nanopore fabrication by controlled dielectric breakdown. PLoS ONE **9**, e92880–e92880. https://doi.org/10.1371/journal.pone.0092880.

[**36**] Bandara, Y. M. N. D. Y., Karawdeniya, B. I., Dutt, S., Kluth, P., and Tricoli, A. (2024). Nanopore fabrication made easy: A portable, affordable microcontroller-assisted approach for tailored pore formation via controlled breakdown. Analytical Chemistry **96**, 2124–2134. https://doi.org/10.1021/acs.analchem.3c04860.

[**37**] Dutt, S., Shao, H., Karawdeniya, B., Bandara, Y. M. N. D. Y., Daskalaki, E., Suominen, H., and Kluth, P. (2023). High accuracy protein identification: Fusion of solid-state nanopore sensing and machine learning. Small Methods **7**, 2300676. https://doi.org/10.1002/smtd.202300676.

[**38**] Dutt, S., Karawdeniya, B., Bandara, Y. M. N. D. Y., and Kluth, P. (2023). Nanopore sensing and machine learning: future of biomarker analysis and disease detection. Future Science OA.

[**39**] Meyer, N., Janot, J.-M., Lepoitevin, M., Smietana, M., Vasseur, J.-J., Torrent, J., and Balme, S. (2020). Machine learning to improve the sensing of biomolecules by

conical track-etched nanopore. Biosensors **10**, 140. https://doi.org/10.3390/bios10100140.

[**40**] Taniguchi, M., Minami, S., Ono, C., Hamajima, R., Morimura, A., Hamaguchi, S., Akeda, Y., Kanai, Y. (2021). Combining machine learning and nanopore construction creates an artificial intelligence nanopore for coronavirus detection. Nature Communications **12**, 3726. https://doi.org/10.1038/s41467-021-24001-2.

[**41**] Arima, A., Tsutsui, M., Washio, T., Baba, Y., and Kawai, T. (2021). Solid-state nanopore platform integrated with machine learning for digital diagnosis of virus infection. Analytical Chemistry **93**, 215–227. https://doi.org/10.1021/acs.analchem.0c04353.

[**42**] Wu, J., Liang, L., Zhang, M., Zhu, R., Wang, Z., Yin, Y., Yin, B., Weng, T. (2022). Single-molecule identification of the conformations of human C-Reactive protein and its aptamer complex with solid-state nanopores. ACS Applied Materials & Interfaces **14**, 12077–12088. https://doi.org/10.1021/acsami.2c00453.

[**43**] Chae, H., Kwak, D.-K., Lee, M.-K., Chi, S.-W., and Kim, K.-B. (2018). Solid-state nanopore analysis on conformation change of p53TAD–MDM2 fusion protein induced by protein–protein interaction. Nanoscale **10**, 17227–17235. https://doi.org/10.1039/C8NR06423G.

[**44**] Hu, R., Rodrigues, J. V., Waduge, P., Yamazaki, H., Cressiot, B., Chishti, Y., Makowski, L., Yu, D. (2018). Differential enzyme flexibility probed using solid-state nanopores. ACS Nano **12**, 4494–4502. https://doi.org/10.1021/acsnano.8b00734.

[**45**] Chau, C., Marcuccio, F., Soulias, D., Edwards, M. A., Tuplin, A., Radford, S. E., Hewitt, E., and Actis, P. (2022). Probing RNA conformations using a polymer–electrolyte solid-state nanopore. ACS Nano **16**, 20075–20085. https://doi.org/10.1021/acsnano.2c08312.

[**46**] Namani, S., Kavetsky, K., Lin, C.-Y., Maharjan, S., Gamper, H. B., Li, N.-S., Piccirilli, J. A., Hou, Y.-M. (2024). Unraveling RNA conformation dynamics in mitochondrial encephalomyopathy, lactic acidosis, and stroke-like episode syndrome with solid-state nanopores. ACS Nano **18**, 17240–17250. https://doi.org/10.1021/acsnano.4c04625.

[**47**] Lee, C., Joly, L., Siria, A., Biance, A.-L., Fulcrand, R., and Bocquet, L. (2012). Large Apparent Electric Size of Solid-State Nanopores Due to Spatially Extended Surface Conduction. Nano Letters **12**, 4037–4044. https://doi.org/10.1021/nl301412b.

[**48**] Ashiotis, G., Deschildre, A., Nawaz, Z., Wright, J. P., Karkoulis, D., Picca, F. E., and Kieffer, J. (2015). The fast azimuthal integration Python library: *pyFAI*. Journal of Applied Crystallography **48**, 510–519. https://doi.org/10.1107/S1600576715004306.

[**49**] Manalastas-Cantos, K., Konarev, P. V., Hajizadeh, N. R., Kikhney, A. G., Petoukhov, M. V., Molodenskiy, D. S., Panjkovich, A., Mertens, H. D. T. (2021). *ATSAS 3.0* : expanded functionality and new tools for small-angle scattering data analysis. Journal of Applied Crystallography **54**, 343–355. https://doi.org/10.1107/S1600576720013412.

[**50**] Cantara, W. A., Olson, E. D., and Musier-Forsyth, K. (2017). Analysis of RNA structure using small-angle X-ray scattering. Methods **113**, 46–55. https://doi.org/10.1016/j.ymeth.2016.10.008.

[**51**] Aguilar, R., Spencer, K. B., Kesner, B., Rizvi, N. F., Badmalia, M. D., Mrozowich, T., Mortison, J. D., Rivera, C. (2022). Targeting Xist with compounds that disrupt RNA structure and X inactivation. Nature **604**, 160–166. https://doi.org/10.1038/s41586-022-04537-z.

[**52**] Punjani, A., Rubinstein, J. L., Fleet, D. J., and Brubaker, M. A. (2017). cryoSPARC: algorithms for rapid unsupervised cryo-EM structure determination. Nature Methods **14**, 290–296. https://doi.org/10.1038/nmeth.4169.

[**53**] Owczarzy, R., Moreira, B. G., You, Y., Behlke, M. A., and Walder, J. A. (2008). Predicting stability of DNA duplexes in solutions containing magnesium and monovalent cations. Biochemistry **47**, 5336–5353. https://doi.org/10.1021/bi702363u.

[**54**] Fragasso, A., Schmid, S., and Dekker, C. (2020). Comparing current noise in biological and solid-state nanopores. ACS Nano **14**, 1338–1349. https://doi.org/10.1021/acsnano.9b09353.

[**55**] Woodson, S. A., and Koculi, E. (2009). "Analysis of RNA folding by native polyacrylamide gel electrophoresis". en. In: *Methods in Enzymology*. Vol. 469. Elsevier, 2009, 189–208. ISBN: 978-0-12-380922-3. https://doi.org/10.1016/S0076-6879(09)69009-1. (Visited on 11/21/2024).

[**56**] Janssen, B. D., Diner, E. J., and Hayes, C. S. (2012). "Analysis of aminoacyl- and peptidyl-tRNAs by gel electrophoresis". en. In: *Bacterial Regulatory RNA*. Ed. by Kenneth C. Keiler. Totowa, NJ: Humana Press, 2012, 291–309. ISBN: 978-1-61779-948-8 978-1-61779-949-5. https://doi.org/10.1007/978-1-61779-949-5_19. (Visited on 11/21/2024).

[**57**] Tan, Z.-J., and Chen, S.-J. (2006). Nucleic acid helix stability: Effects of salt concentration, cation valence and size, and chain length. Biophysical Journal **90**, 1175–1190. https://doi.org/10.1529/biophysj.105.070904.

[**58**] Das, N., Chakraborty, B., and RoyChaudhuri, C. (2022). A review on nanopores based protein sensing in complex analyte. Talanta **243**, 123368. https://doi.org/10.1016/j.talanta.2022.123368.

[**59**] Talaga, D. S., and Li, J. (2009). Single-molecule protein unfolding in solid state nanopores. Journal of the American Chemical Society **131**, 9287–9297. https://doi.org/10.1021/ja901088b.

[**60**] Sato, K., Hamada, M., Asai, K., and Mituyama, T. (2009). CENTROIDFOLD: a web server for RNA secondary structure prediction. Nucleic Acids Research **37**, W277–W280. https://doi.org/10.1093/nar/gkp367.

[**61**] Popenda, M., Szachniuk, M., Antczak, M., Purzycka, K. J., Lukasiak, P., Bartol, N., Blazewicz, J., and Adamiak, R. W. (2012). Automated 3D structure composition for large RNAs. Nucleic Acids Research **40**, e112–e112. https://doi.org/10.1093/nar/gks339.

[**62**] Shi, H., and Moore, P. B. (2000). The crystal structure of yeast phenylalanine tRNA at 1.93 å resolution: A classic structure revisited. RNA **6**, 1091–1105. https://doi.org/10.1017/S1355838200000364.

[**63**] Leamy, K. A., Yennawar, N. H., and Bevilacqua, P. C. (2017). Cooperative RNA folding under cellular conditions arises from both tertiary structure stabilization and secondary structure destabilization. Biochemistry **56**, 3422–3433. https://doi.org/10.1021/acs.biochem.7b00325.

[**64**] Meng, E. C., Goddard, T. D., Pettersen, E. F., Couch, G. S., Pearson, Z. J., Morris, J. H., and Ferrin, T. E. (2023). UCSF ChimeraX: Tools for structure building and analysis. Protein Science **32**, e4792. https://doi.org/10.1002/pro.4792.

[**65**] Dyer, K. N., Hammel, M., Rambo, R. P., Tsutakawa, S. E., Rodic, I., Classen, S., Tainer, J. A., and Hura, G. L. (2014). "High-throughput SAXS for the characterization of biomolecules in solution: A practical approach". en. In: *Structural genomics: general applications*. Ed. by Yu Wai Chen. Totowa, NJ: Humana Press, 2014, 245–258. ISBN: 978-1-62703-691-7. https://doi.org/10.1007/978-1-62703-691-7_18.

[**66**] Burger, V. M., Arenas, D. J., and Stultz, C. M. (2016). A structure-free method for quantifying conformational flexibility in proteins. Scientific Reports **6**, 29040. https://doi.org/10.1038/srep29040.

[**67**] Meng, E. C., Goddard, T. D., Pettersen, E. F., Couch, G. S., Pearson, Z. J., Morris, J. H., and Ferrin, T. E. (2023). ¡span style="font-variant:small-caps;"¿UCSF ChimeraX¡/span¿ : Tools for structure building and analysis. Protein Science **32**, e4792. https://doi.org/10.1002/pro.4792.

[**68**] Chen, X., Wang, L., Xie, J., Nowak, J. S., Luo, B., Zhang, C., Jia, G., Zou, J. (2024). RNA sample optimization for cryo-EM analysis. Nature Protocols. https://doi.org/10.1038/s41596-024-01072-1.

[**69**] Wang, L., Xie, J., Gong, T., Wu, H., Tu, Y., Peng, X., Shang, S., Jia, X. (2025). Cryo-EM reveals mechanisms of natural RNA multivalency. Science, eadv3451. https://doi.org/10.1126/science.adv3451.

[**70**] Biela, A., Hammermeister, A., Kaczmarczyk, I., Walczak, M., Koziej, L., Lin, T.-Y., and Glatt, S. (2023). The diverse structural modes of tRNA binding and recognition. Journal of Biological Chemistry **299**, 104966. https://doi.org/10.1016/j.jbc.2023.104966.

[**71**] Moura, T. R. de, Purta, E., Bernat, A., Martín-Cuevas, E. M., Kurkowska, M., Baulin, E. F., Mukherjee, S., Nowak, J. (2024). Conserved structures and dynamics in 5-proximal regions of Betacoronavirus RNA genomes. Nucleic Acids Research **52**, 3419–3432. https://doi.org/10.1093/nar/gkae144.

[**72**] Kappel, K., Zhang, K., Su, Z., Kladwang, W., Li, S., Pintilie, G., Topkar, V. V., Rangan, R. (2019). *Ribosolve: Rapid determination of three-dimensional RNA-only structures*. 2019. https://doi.org/10.1101/717801. (Visited on 04/04/2025).

[**73**] Zhang, K., Li, S., Kappel, K., Pintilie, G., Su, Z., Mou, T.-C., Schmid, M. F., Das, R. (2019). Cryo-EM structure of a 40 kDa SAM-IV riboswitch RNA at 3.7 å resolution. Nature Communications **10**, 5511. https://doi.org/10.1038/s41467-019-13494-7.

[**74**] Zhang, K. (2021). Cryo-EM and antisense targeting of the 28-kDa frameshift stimulation element from the SARS-CoV-2 RNA genome. Molecular Biology **28**.

[**75**] Ganser, L. R., Kelly, M. L., Herschlag, D., and Al-Hashimi, H. M. (2019). The roles of structural dynamics in the cellular functions of RNAs. Nature Reviews Molecular Cell Biology **20**, 474–489. `https://doi.org/10.1038/s41580-019-0136-0`.

[**76**] Roh, J. H., Tyagi, M., Aich, P., Kim, K., Briber, R. M., and Woodson, S. A. (2015). Charge screening in RNA: an integral route for dynamical enhancements. Soft Matter **11**, 8741–8745. `https://doi.org/10.1039/C5SM02084K`.